Application of Gauss's Theorem to quantify localized surface emissions from airborne measurements of wind and trace gases

Stephen Conley*[1,6], Ian Faloona[1], Shobhit Mehrotra[1], Maxime Suard[1], Donald H. Lenschow[2], Colm Sweeney[4], Scott Herndon[3], Stefan Schwietzke[4,5], Gabrielle Pétron[4,5], Justin Pifer[6], Eric A. Kort[7] and Russell Schnell[5]

[1]Department of Land, Air, & Water Resources, University of California, Davis, 95616, USA
[2]Mesoscale and Microscale Meteorology Laboratory, National Center for Atmospheric Research, Boulder, Colorado, 80307, USA
[3]Aerodyne Research, Inc, Billerica, Massachusetts, 01821, USA
[4]Cooperative Institute for Research in Environmental Sciences, University of Colorado, Boulder, Colorado, 80305, USA
[5]NOAA Earth System Research Laboratory, Boulder, Colorado, USA
[6]Scientific Aviation, Inc., Boulder, CO, USA
[7]Climate and Space Sciences and Engineering, University of Michigan

Correspondence to: S. A. Conley (saconley@ucdavis.edu)

1   **Abstract**
2   Airborne estimates of greenhouse gas emissions are becoming more prevalent with the advent of
3   rapid commercial development of trace gas instrumentation featuring increased measurement
4   accuracy, precision, and frequency, and the swelling interest in the verification of current emission
5   inventories. Multiple airborne studies have indicated that emission inventories may underestimate
6   some hydrocarbon emission sources in U.S. oil and gas producing basins. Consequently, a proper
7   assessment of the accuracy of these airborne methods is crucial to interpreting the meaning of such
8   discrepancies. We present a new method of sampling surface sources of any trace gas for which fast
9   and precise measurements can be made and apply it to methane, ethane, and carbon dioxide on
10   spatial scales of ~1000 m, where consecutive loops are flown around a targeted source region at
11   multiple altitudes. Using Reynolds decomposition for the scalar concentrations, along with Gauss's
12   Theorem, we show that the method accurately accounts for the smaller scale turbulent dispersion of
13   the local plume, which is often ignored in other average "mass balance" methods. With the help of
14   large eddy simulations (LES) we further show how the circling radius can be optimized for the
15   micrometeorological conditions encountered during any flight. Furthermore, by sampling controlled
16   releases of methane and ethane on the ground we can ascertain that the accuracy of the method, in
17   appropriate meteorological conditions, is often better than 10%, with limits of detection below 5 kg
18   hr^{-1} for both methane and ethane. Because of the FAA mandated minimum flight safe altitude of 150
19   m, placement of the aircraft is critical to preventing a large portion of the emission plume from
20   flowing underneath the lowest aircraft sampling altitude, which is generally the leading source of
21   uncertainty in these measurements. Finally, we show how the accuracy of the method is strongly
22   dependent on the number of sampling loops, or time spent sampling the source plume.

24   # 1   Introduction

25   Accurate national inventories of greenhouse gas emissions (primarily carbon dioxide (CO_2), methane
26   (CH_4), and nitrous oxide (N_2O)) is of paramount importance in developing strategies to understand
27   global emissions. The multitude of sources, however, are so often highly variable in area, emission
28   magnitude, height above ground, and duration that rigorous verification is exceedingly difficult.
29   Nevertheless, measurement techniques have improved markedly in the past decade, and these are
30   being employed to an unprecedented extent in an effort to evaluate and refine emission inventories
31   (Nisbet and Weiss, 2010). Most so called "bottom-up" inventories are developed by aggregating
32   statistical correlates of individual process emissions to such mapping variables as population density,
33   energy consumption, head of cattle, etc., extrapolating to total emissions using a relatively small
34   number of direct measurements. On the other hand, atmospheric scientists have long striven to use
35   measurements from global surface networks, aircraft campaigns, and satellites to try to determine
36   emissions based on the amounts and build-up rates of observed trace gases. Aircraft and satellites,
37   the "top-down" approach, conveniently integrates the multitude of sources, but is heavily reliant on a
38   detailed knowledge of atmospheric transport. Top-down methods also suffer from difficulties
39   attributing sources and generalizing measurements made over a relatively short time period.
40   Attempts to reconcile these two distinct methods on global (Muhle et al., 2010) and continental
41   scales (Gerbig et al., 2003; Miller et al., 2013) have often indicated an apparent underestimation by
42   the "bottom-up" methods of a factor 1.5 or more.

43   In principle, the aircraft top-down measurements can be conducted at all the atmospheric scales to
44   better understand and identify the emissions at comparable scales. For long-lived greenhouse gases,
45   which readily disperse throughout the atmosphere, the global scale is very instructive. The seminal
46   experiment began with Keeling's acclaimed CO_2 curve [1960], and has continued through more
47   contemporary techniques by Hirsch et al.(2006) and Neef et al. (2010) for CH_4 and N_2O, respectively.
48   At progressively smaller scales more details of the source strengths and apportionment can be made:
49   from synoptic or continental scales which can help constrain national inventories (Bergamaschi et al.,
50   2005) or specific biogeographic regions (Gallagher et al., 1994), to mesoscale investigations that
51   estimate emissions from urban areas (Mays et al., 2009; Turnbull et al., 2011; Wecht et al., 2014) or
52   specific oil and gas producing fields (Karion et al., 2013; Petron et al., 2014) and even down to
53   individual point/area sources on the order of 10-100 m size (Denmead et al., 1998; Lavoie et al., 2015;
54   Roscioli et al., 2015).

55   Aircraft in-situ measurements are particularly useful for "top-down" methods at the sub-mesoscale
56   because they can be used to measure the air both upwind and downwind of a source region.
57   However, deployments tend to be costly and thus sporadic. As far as we know, the aircraft methods
58   used so far can be categorized into three types. First, there is the eddy covariance technique that is
59   carried out at low altitudes wherein the vertical fluxes of gases carried by the turbulent wind are
60   measured by tracking rapid fluctuations of both concentrations and vertical wind (Hiller et al., 2014;
61   Ritter et al., 1994; Yuan et al., 2015). This method is generally thought to be the most direct, but it is
62   limited to small footprint regions which must be repeatedly sampled for sufficient statistical
63   confidence, requires a sophisticated vertical wind measurement, and can be subject to errors due to
64   flux divergence between the surface and the lowest flight altitude and acceleration sensitivity of the
65   gas sensor. The second, and by far the most common approach is what chemists usually refer to as
66   "mass balance" and what is known in the turbulence community as a "scalar budget" technique.
67   Many different sets of assumptions and sampling strategies are employed, but the overall goal is to
68   sample the main dispersion routes of the surface emissions as they make their way into the overlying
69   atmosphere after first accumulating near the surface. The scales that can be addressed by this
70   method are from a few kilometers (Alfieri and Blanken, 2012; Hacker et al., 2016; Hiller et al., 2014;
71   Tratt et al., 2014) to tens of kilometers (Caulton et al., 2014; Karion et al., 2013; Wratt et al., 2001) to
72   even potentially hundreds of kilometers (Beswick et al., 1998; Chang et al., 2014), and this approach
73   has been the focus of recent measurements in natural gas production basins. These basins present a
74   source apportionment challenge in that emissions from multiple sources (agriculture, oil & gas wells,
75   geologic seepage, etc.) commingle as the air mass travels across the basin. The third method of
76   source quantification is to reference measurements of the unknown trace gas to a reference trace
77   gas with a metered release (tracer) or otherwise known emission rate and assume that the tracer and
78   the scalar of interest have the same diffusion characteristics. Typically this tracer release technique is
79   applied to small scales of tens to hundreds of meters (Czepiel et al., 1996; Lamb et al., 1995; Roscioli
80   et al., 2015), but the principle has been attempted at the basin (Peischl et al., 2013) and continental
81   (Miller et al., 2012) scales using a reference trace gas with a suitable known emission rate such as CO_2
82   or CO.

83   The airborne mass balance flight strategies can be grouped into three basic patterns: a single height
84   transect around a source assuming a vertically uniformly mixed boundary layer (Karion et al., 2013);
85   single height upwind/downwind (Wratt et al., 2001) or sometimes just downwind flight legs (Conley

86 et al., 2016; Hacker et al., 2016; Ryerson et al., 1998); and multiple flight legs at different altitudes,
87 (Alfieri et al., 2012; Gordon et al., 2015; Kalthoff et al., 2002); or just a 'screen' on the downwind face
88 of the box (Karion et al., 2015; Lavoie et al., 2015; Mays et al., 2009).

89 Here we describe a new airborne method borne out of a necessity to identify and quantify source
90 emissions to within 20% accuracy in a large heterogeneous field of potential sources. The novel
91 technique applies an aircraft flight pattern that circumscribes a virtual cylinder around an emission
92 source and, using only observed horizontal wind and trace gas concentrations, applies Gauss's
93 Theorem to estimate the flux divergence through that cylinder. By integrating the outward horizontal
94 fluxes at each point along the circular flight path, the flux contributions from enclosed sources can be
95 accounted for. Making an accurate estimate, however, requires the selection of an appropriate
96 circling radius based on the micrometeorological conditions inferred in flight from measurements
97 onboard the aircraft. The pattern must be far enough downstream for the plume to mix sufficiently in
98 the vertical, yet not so far that the trace gas plume enhancements do not stand out sufficiently from
99 the background concentration.

100 In this study we first present the general analytical method used to derive emission estimates using
101 airborne measurements. Next, we investigate the structure of a generalized dispersing plume using
102 large-eddy simulation (LES) to better understand the optimal sampling strategies for quantifying
103 near-surface gas sources. Because the wind fields of turbulent flows cannot be predicted in detail, we
104 do not attempt to compare specific features of our observations with specific LES results, but rather
105 we use the numerical experiments to guide the development of the observational methodology. For
106 example, by investigating the LES flux divergence profiles in the layer below the lowest flight altitude,
107 we are able to estimate the contribution of this unmeasured component to the overall source
108 strength. We then evaluate the accuracy of the approach using coordinated planned release
109 experiments and by applying the method to CO_2 emitted from several power plant plumes to
110 compare with reported emissions.

111

2 Data Collection

2.1 Airborne Instrumentation

114 The airborne detection system is flown on a fixed wing single-engine Mooney aircraft, extensively
115 modified for research as described in Conley et al. (2014). Ambient air is collected through ~5 m of
116 tubing (Kynar, Teflon and stainless steel) that protrudes out of backward-facing aluminum inlets
117 mounted below the right wing. In-situ CH_4, CO_2, and water vapor are measured with a Picarro 2301f
118 cavity ring down spectrometer as described by Crosson (2008), which is operated in its precision
119 mode at 1 Hz. In-situ ethane (C_2H_6) is measured with an Aerodyne Methane/Ethane tunable diode
120 infrared laser direct absorption spectrometer (Yacovitch et al., 2014). There is a 5-10 second time lag
121 in both analyzers that depends on the flow rate and tubing diameter. We use a 1/8" OD (3.175 mm)
122 stainless line for the Picarro (~0.2 slpm flow rate), and a 6.3 mm (¼ in) Teflon line for the CH_4/ C_2H_6
123 spectrometer (~4 slpm flow rate). This results in lag times of ~5 s for the Aerodyne and ~10 s for the
124 Picarro. The lag time for the Picarro is calculated using a "breath test", whereby we exhale into the air
125 inlet and measure the time required for the CO_2 measurement to peak. The ethane lag time is

126 adjusted to maximize the correlation between the ethane and Picarro methane time series in plumes
127 where both gases are emitted. Both lag times are slightly dependent on pressure, i.e., with a typical
128 altitude change of ~1 km, the change in lag time is less than 10%, and is inconsequential when
129 applying this method within a few hundred meters from the surface. The horizontal wind speed and
130 direction, sampled at 1 Hz, is based on a standard aircraft pitot-static pressure airspeed measurement
131 and a dual GPS compass that determines aircraft heading and ground speed. The accuracy of the
132 horizontal wind measurement is about 0.2 m s^{-1} (Conley et al., 2014). The horizontal wind is
133 calibrated periodically by flying ~5 km L-shaped patterns in the free troposphere; a heading rotation
134 and airspeed adjustment is made to the wind calculation to minimize the dependence of the wind on
135 aircraft heading. These adjustments typically amount to less than 2° rotation and 3% adjustment of
136 the airspeed. In flying the tight circle patterns described below, the pilot does not adjust the rudder
137 trim to use the same calibration coefficients in the wind measurement calculation throughout the
138 flight.

139 **2.2   Large Eddy Simulations**

140 In order to study the plume behaviour of surface emissions as it relates to sampling in the stacked
141 circles, we use the LES module of *WRF V3.6.1*. *WRF-LES* explicitly resolves the largest turbulent eddies
142 by filtering the Navier-Stokes scalar conservation equations at some scale in the inertial subrange,
143 and allowing the smaller motions beyond the cut-off to be modeled using a sub-grid (also called a
144 subfilter) scale turbulence parameterization that is based on properties of the larger-scale, resolved
145 flow. Because the aircraft data is typically sampled at 1 Hz and the true airspeed is around 70 m s^{-1},
146 we use an LES horizontal grid size roughly half (40 and 50 m) the distance between aircraft data
147 samples. Because periodic lateral boundary conditions are imposed on the WRF-LES variables, care
148 must be taken to ensure that the effluent does not reach the lateral boundaries of the simulation
149 domain. On the other hand, WRF-LES does not allow for parallelized computation, making the
150 simulations quite expensive in terms of computation time. We therefore struck a balance between a
151 large enough domain in horizontal extent (6 and 8 km) such that the effluent would not reach the
152 downwind boundary before the end of our simulation, while maintaining a grid size small enough to
153 resolve scales of the aircraft observations. The vertical domain needs to be large enough to
154 encompass a developing convective boundary layer (CBL), while at the same time containing
155 substantial free tropospheric flow above to serve as a reservoir that can feed momentum and free-
156 tropospheric scalars to the CBL. Moreover, the stable region (potential temperature lapse rate $d\theta/dz$
157 = 5 C km^{-1}) between the CBL inversion base and the top of the domain had to be large enough to
158 damp any wave activity before it could reflect off the upper boundary and create spurious motions
159 throughout the domain.

160 The standard *WRF-LES* module is not set up to allow for effluent release, so we implemented a
161 modified version of the *WRF* source code (*S.-H. Chen, personal communication*) that includes a
162 surface effluent release with a specified position and release rate. Three different convective
163 simulations were run with varying resultant mean wind speeds in the boundary layer, and each was
164 allowed 4-5 hours to 'spin-up' dynamically before the effluent was released at a rate of between 2.9-
165 3.5 kg hr^{-1}. The exact release time was selected to give reasonably stationary CBL depths and
166 turbulent kinetic energy. The conditions for the three simulations are listed in Table 1, and based on

167   the different wind speeds they span moderate to strongly convective boundary layers ($-z_i/L_{MO}$ from
168   ~50 to ~200, where L_{MO} is the Monin-Obukhov length and z_i is the CBL depth.)

169   **3   Methods**

170   **3.1   Theory of Measurement using Gauss's Theorem**

171   We use an integrated form of the scalar budget equation for a passive, conservative scalar in a
172   turbulent fluid to estimate the emission of a gas of interest within a cylindrical volume V. The volume
173   is circumscribed by a series of closed aircraft flight paths (typically circular) flown around the emission
174   source over a range of altitudes. The altitudes encompass the lowest safe flight level (usually 75-150
175   mAGL) up to an altitude where no discernable change in the trace gas mixing ratio, χ, is observed
176   around the flight loop, z_{max}. The scalar in our case is the mass concentration (i.e., density of a
177   chemically unreactive species in a turbulent flow field, $\boldsymbol{u} = u\boldsymbol{i}+v\boldsymbol{j}+w\boldsymbol{k}$; its Reynolds decomposition is $c = $
178    $C + c'$, where C is the mean concentration around each loop and c' is the departure from the loop
179   mean. Figure 1 shows an actual example of the effluent sampled by the aircraft in a sequence of
180   stacked paths l that circumscribe an area, A, enclosing the source in a volume, V. The effluent is
181   carried downwind as it mixes upward in the CBL. A virtual surface circumscribed by the circular flight
182   tracks is assumed enclosing the source and extending above the vertical extent of the plume so that
183   there is no vertical transport above that level. To estimate the source strength, we start with the
184   integral form of the continuity equation:

$$Q_c = \langle \frac{\partial m}{\partial t} \rangle + \iiint \nabla \cdot c\boldsymbol{u}\, dV \qquad (1)$$

185   where $\langle\ \rangle$ denotes an average over the volume V, Q_c is the sum of the internal sources and sinks of c
186   within V, and m is the total mass of c within the volume V. At this point, we recognize that the flux
187   divergence is composed of two terms

$$\boldsymbol{\nabla} \cdot c\mathbf{u} = \boldsymbol{u} \cdot \nabla c + c\nabla \cdot \mathbf{u} \qquad (2)$$

188

189   In section 3.2 we perform a scale analysis of the terms on the right-hand side (rhs) of equation 2 and
190   show that the second term, which is proportional to the horizontal wind divergence, may be
191   neglected under our normal flight protocol. This is fortunate because of the difficulty in accurately
192   estimating the horizontal wind divergence from aircraft measurements (Lenschow et al., 2007). The
193   vertical flux across the top of the flight cylinder is assumed to be zero and the flux from the bottom
194   (ground) is the surface source we are measuring. This leaves us with only the horizontal flux, i.e. $c\boldsymbol{u_h}$
195   where $\boldsymbol{u_h}$ (= $u\mathbf{i}+v\mathbf{j}$). In order to minimize the contribution from the horizontal wind divergence term,
196   we remove the loop mean concentration, C, which does not alter the first term on the rhs because
197   ∇C =0, so that equation 2 becomes

$$\boldsymbol{u_h} \cdot \nabla c + c\nabla \cdot \boldsymbol{u_h} = \boldsymbol{u_h} \cdot \nabla(c'). \tag{3}$$

198   Next, we use Gauss's Theorem to relate the volume integral to a surface integral around the volume
199   that is sampled by the aircraft flight loops:

$$Q_c = \langle \frac{\partial m}{\partial t} \rangle + \iiint \nabla \cdot (c'\boldsymbol{u}) \, dV = \langle \frac{\partial m}{\partial t} \rangle + \oiint c'\boldsymbol{u} \cdot \hat{\boldsymbol{n}} \, dS \tag{4}$$

200   where S is the surface enclosing V and $\hat{n}$ is an outward pointing unit vector normal to the surface.

201   The surface integral can be broken into three elements: a cylinder extending from the ground up to a
202   level above significant modification by the emission, the ground surface circumscribed by a low-level
203   (virtual) circular flight path ($z = 0$), and a nominally horizontal surface circumscribed by a flight path
204   above the level modified by the source ($z = z_{max}$). We assume there is no significant flux (other than
205   the source of interest) into or out of the ground. Next, the surface integral is estimated solely from a
206   sequence of closed path integrals measured by the aircraft at multiple flight levels to estimate the
207   right side of Eq. 5 (blue dashed lines in Fig. 1),

$$\oiint c'\boldsymbol{u} \cdot \hat{\boldsymbol{n}} \, dS = \int_0^{z_{max}} \oint c'\boldsymbol{u_h} \cdot \hat{\boldsymbol{n}} dl \, dz, \tag{5}$$

208   where l is the flight path.

209

210   Combining Eqs. 4 and 5 leads to the result that is the basis for this measurement technique where a
211   series of horizontal loops at different altitudes are flown around a source region:

$$Q_c = \langle \frac{\partial m}{\partial t} \rangle + \int_0^{z_{max}} \oint c'\boldsymbol{u_h} \cdot \hat{\boldsymbol{n}} dl \, dz \tag{6}$$

212   Along each path the instantaneous outward flux is computed and summed over the loop to yield the
213   mean flux divergence via Gauss's Theorem. A temporal trend of the total mass within the volume
214    $(\frac{\partial m}{\partial t})$ can be estimated from the flight data and added to the flux divergence integral to obtain the
215   emission rate.

216

217   **3.2 Divergence Uncertainty**

218   In order to estimate the relative error in the horizontal divergence term that we are eliminating, we
219   perform a scale analysis of the relative size of the two terms in Eq. 2, using some typical values of the
220   CBL parameters (convective velocity scale $w_* = 1 \text{ m } s^{-1}$, boundary layer depth, z_i = 1,000 m), and
221   sampling geometry (flying at a radius 1 km around a point source.) Taylor's (1922) statistical theory of
222   dispersion in a homogenous and stationary turbulent fluid predicts that the root mean square lateral
223   (σ_y) and vertical (σ_z) dispersion parameters increase linearly with time, or equivalently advection
224   distance, downwind in the near-field. Weil (1988) shows several examples of the growth of both of
225   these parameters downwind to be ~ $0.5w_*$, which we use here for a rough estimate of a conical

226 plume spreading to quantify the dilution of the source's emission as it travels downwind to be
227 intercepted by the aircraft. We use a large background mixing ratio characteristic of global CH_4 (~1.9
228 ppmv), estimate the mean gradient by the plume concentration divided by the distance downwind,
229 and assume a conservatively large horizontal wind divergence of 10^{-5} s^{-1}, which may in fact be typical
230 for our small sampling region (Stull, 1988). The results are shown in Figure 2 and, for all but the
231 smallest sources of a few kg hr^{-1} and wind speeds below 1 m s^{-1}, the divergence term is at least an
232 order of magnitude smaller than the gradient term.

233

3.3 Applying the Theory to the LES Results

235 We calculated a comparable estimate of Q_c in the LES domain from the air density, concentration,
236 and wind along circular flight paths as a virtual aircraft would fly. Willis and Deardorff (1976)
237 generalized results of their convection tank experiments to downwind dispersion in the convective
238 boundary layer (CBL) in terms of a dimensionless length scale X, the ratio of the horizontal advection
239 time to the large eddy turnover time:

$$X = \frac{x w_*}{U z_i} \qquad (7)$$

240 where x is the downwind distance and U is the vertically averaged mean wind speed.

241 Figure 3 shows the crosswind-integrated concentration profile for the plume release in the UCD50B
242 WRF-LES run as function of X, and normalized height, $Z = z/z_i$. Because of the time limitation due to
243 the periodic boundary conditions, the plume is averaged for only ~15 minutes of simulation time
244 which is just under a large eddy turnover time for the conditions of the run. The results displayed in
245 Figure 3 are in good qualitative agreement with the results of Willis and Deardorff (1976) and Weil et
246 al., (2012) save for the release being at the surface in our LES study, and at $Z = 0.067$ for the above
247 studies (see Fig. 1 and 2 of Weil et al., (2012)). Figure 3 shows the maximum concentration being
248 lofted near X~0.2 and leveling off near $Z \sim 0.8$ around $X \sim 0.6$; beyond $X > 1.5$ the plume is fairly well-
249 mixed throughout the extent of the boundary layer.

3.4 The Upwind Directed Turbulent Flux

251 Horizontal turbulent fluxes are generally ignored in boundary layer budget studies due to the fact
252 that while they are often sizeable in magnitude they do not change significantly over horizontal
253 length scales under consideration (the horizontal homogeneity assumption). In the vicinity of a point
254 source, however, this is not likely. The method outlined here estimates source emissions using a
255 measured horizontal flux that incorporates wind and scalar measurements at 1 Hz sample rate,
256 resolving scales of ~70 m (Conley et al., 2014), which should include nearly all of the turbulent
257 contributions to the horizontal flux. Here we consider the nature of this turbulent flux and the error
258 in emission estimates if only the mean transport were considered. We start with the budget equation
259 for a horizontal scalar flux in a horizontally homogeneous turbulent flow where the molecular
260 diffusive/viscous term has been neglected (Wyngaard, 2010),

261
$$\frac{d\overline{c'u'}}{dt} = -\overline{u'^2}\frac{\partial C}{\partial x} - \overline{u'w'}\frac{\partial C}{\partial z} - \overline{c'w'}\frac{\partial U}{\partial z} - \frac{\partial \overline{c'u'^2}}{\partial x} - \frac{\partial \overline{c'u'w'}}{\partial z} - \frac{1}{\rho}\overline{c'\frac{\partial p'}{\partial x}}$$
(8)

262 where ρ is density and p' is the pressure fluctuation. We then assume stationarity and integrate
263 across the source from a point just upwind to a point within the plume and obtain

264
$$\int_{0-}^{x}\frac{\partial \overline{c'u'}}{\partial x'}dx' = -\frac{1}{U}\int_{0-}^{x}\left[\overline{u'^2}\frac{\partial C}{\partial x'} + \overline{u'w'}\frac{\partial C}{\partial z} + \overline{c'w'}\frac{\partial U}{\partial z} + \frac{\partial \overline{c'u'^2}}{\partial x'} + \frac{\partial \overline{c'u'w'}}{\partial z} + \frac{1}{\rho}\overline{c'\frac{\partial p'}{\partial x'}}\right]dx'$$
(9)

265 We further assume that although the scalar field is not homogeneous the flow field is, and the
266 background horizontal c-flux upwind is much smaller than the flux induced by the point source. This
267 results in an equation for the in-plume flux

268
$$\overline{c'u'} = -\frac{1}{U}\left[\overline{u'^2}(C_x - C_{bckg}) + \overline{u'w'}\int_{0-}^{x}\frac{\partial C}{\partial z}dx' + \int_{0-}^{x}\overline{c'w'}\frac{\partial U}{\partial z} + \int_{0-}^{x}\left(\frac{\partial \overline{c'u'^2}}{\partial x'} + \frac{\partial \overline{c'u'w'}}{\partial z} + \frac{1}{\rho}\overline{c'\frac{\partial p'}{\partial x'}}\right)dx'\right]$$
(10)

269 The first three terms on the rhs of equation 10 are negative within the plume with their largest
270 magnitudes on the upwind side and diminishing downwind. On the largest, boundary layer filling
271 eddy scales the mean concentration of C downwind of a source is greater than in the upwind region,
272 (C_x-C_{bckg})>0, and therefore the first term is negative, but decreases in magnitude with distance
273 downwind. However, this term is also positive on smaller scales within the plume where the mean
274 gradient is directed upwind towards the source, and is most likely responsible for the specious
275 intuitive impression that the horizontal turbulent flux should transport the plume downwind from the
276 source along with the mean wind advection. Moreoever, the second and third terms on the rhs are
277 negative because the momentum flux, $\overline{u'w'}$, and mean vertical gradient, $\partial C/\partial z$, are negative while the
278 vertical turbulent flux, $\overline{c'w'}$, and wind shear,$\partial U/\partial z$, are positive. Based on the vertical concentration
279 profiles shown in Weil et al. (2012) (their Figures 3 & 4) it can be inferred that the vertical
280 concentration gradient, $\partial C/\partial z$, changes from negative to positive near X~1 and becomes negligible for
281 X > 2-3. Similarly, in the third term, the vertical flux, $\overline{c'w'}$, decreases with fetch. Thus the counter-
282 directed flux ($\overline{c'u'} < 0$) will fade with distance downwind. Wyngaard et al. (1971) have shown that
283 the third-moment, turbulent transport terms (4 and 5 on rhs of equation 10) in the horizontal heat
284 flux equation are small in the surface layer compared to the source terms, so we assume the same
285 holds for this scalar flux. Finally, the remaining pressure covariance term is believed to be the main
286 sink in the budget equation working to decorrelate the wind and the scalar as was shown in the
287 surface layer measurements of Wilczak and Bedard (2004). Therefore, the dominant production
288 terms for negative $\overline{c'u'}$ (terms 1-3 on the rhs of 10) must be balanced by the pressure-correlation
289 term leading to an upwind-directed horizontal turbulent flux within the plume that decreases in
290 magnitude in the downwind direction.

291 This conclusion is supported by several previous studies. For example, in a wind-tunnel study of flux-
292 gradient relationships Raupach & Legg (1984) reported that the mean streamwise horizontal heat flux
293 calculated by multiplying the mean wind by the mean temperature overestimates the total heat flux
294 by approximately 10%, which suggests that the turbulent component of the horizontal heat flux is
295 negative; that is, the turbulent flux is upwind, directed counter to the mean flow. Other researchers
296 have reported an even larger disparity. Field experiments by Leuning et al. (1985) indicate that the
297 horizontal turbulent flux of a trace gas is ~15% the mean flux, while Wilson and Shum (1992) suggest
298 it may be 20%. A recent LES study of particle dispersion over a plant canopy by Pan et al. (2014)

299 indicates magnitudes of 20% or more for the negative turbulent component of scalar fluxes in the
300 vicinity of the source and decreasing with downwind fetch. We therefore conclude that when
301 sampling a near-surface point source at X of order unity or less, if only the mean concentration
302 difference is measured, a significant overestimate of the scalar source is likely to occur.

303 Further evidence of this is shown in the average cospectrum of the outward wind and concentration
304 fluctuation observed in the flight loops in Figure 4. Because the integral of the cospectrum yields the
305 total flux (scalar and wind covariance), this function is useful for examining the contributions to the
306 overall flux from each of the scales of motion (represented by aircraft speed divided by frequency).
307 The results shown in Figure 4 are from a CH_4 point source with an estimated emission rate of 46 $\pm$7 kg
308 hr^{-1} which was circled 70 times at a dimensionless radius X of approximately 0.35. All cospectra of
309 sampled sources have the same structure seen in Figure 4: there is an obvious peak at the mean flight
310 loop frequency (usually ~100 s period) followed by a smaller negative dip at higher frequencies within
311 the meandering effluent plume. We believe this to be good evidence that our method captures this
312 important component of the overall flux away from the source, which cannot be obtained with a
313 traditional mean wind and an integrated concentration enhancement measurement that is so often
314 employed in airborne source estimates (Ryerson et al., 2001; White et al., 1976).

3.5 Choosing the Downwind Sampling Distance

316 Determining the optimal sampling distance from the targeted point source is a balance of several
317 factors. First, not surprisingly, the largest plume signal occurs closest to the source (Figure 3). Second,
318 a high degree of confidence in the results is contingent upon sampling the majority of the plume at
319 and above the lowest flight altitude, which only occurs downwind after a sufficient time has elapsed
320 to loft the initially near-surface plume. And third, an attempt is made to sample the plume before it
321 reaches the top of the boundary layer so that the vertical turbulent entrainment flux does not
322 become appreciable violating the assumption of negligible flux through the top of the volume V as
323 discussed in Equation 2. Finally, close to the source, the fluctuations in concentration will be very
324 large, intermittent, at small scales, and highly variable.

325 To gain further insight into the second feature of the dispersing plume, Figure 5 shows the average
326 horizontal flux divergence profiles derived from the three WRF-LES runs. Here we discuss a
327 dimensionless R, which is identical to X, to emphasize that this scaled downwind distance from the
328 source is a radius of a flight loop. The flux divergence values are made dimensionless by the boundary
329 layer height, z_i, and the source emission rate, Q. Very close to the source, before the plume has had a
330 chance to loft, the flux divergence profile exhibits a strong gradient below the minimum safe flight
331 altitude, making that term difficult to measure directly, as shown in Figure 5. Farther from the source,
332 the signal becomes weaker with increasing altitude and eventually becomes increasingly influenced
333 by entrainment fluxes. We therefore seek a sampling distance that is far enough to allow sufficient
334 vertical lofting yet close enough so that plume crossings are easily observable against the background
335 variability and instrument noise, and are not yet influenced by entrainment mixing.

336 Based on the simulation results presented in Figure 5, we see the gradient below the lowest flight
337 safe altitude typically becomes very small for R > 0.4, and therefore we attempt to target that
338 distance to minimize the extrapolation error from the flight data to the surface. We do not currently

339   measure all the necessary parameters to estimate R in-flight (primarily the surface heat flux $\overline{(w'\theta'_v)}_0$
340   which is required to estimate w∗). Instead, we estimate w_* based on the observed boundary layer
341   height, standard deviation of wind speed, and a parameterization for $w_* = \sigma_u$ /0.6 *(Caughey and*
342   *Palmer, 1979).*

3.6 Minimum number of passes

344   The atmospheric boundary layer is a turbulent medium, meaning that two passes across a plume at
345   the same altitude and distance downwind will likely make very different measurements of the trace
346   gases of interest. A natural question arises as to how many passes are required to develop a
347   statistically sound estimate of the emission rate. We investigate the number of passes required to
348   obtain a statistically robust estimate using the WRF-LES results and a controlled release experiment.
349   By calculating the horizontal flux divergences with a virtual airplane flying through the simulated
350   tracer field, and then randomly sampling the flux divergences from each of the legs and plotting the
351   resultant estimated emission rate as a function of the number of samples used we obtain the results
352   presented in Figure 6. The gray region around the red line mean represents the standard deviation of
353   estimates based on a random set of loops. Figure 7 shows results from an analysis of actual flight data
354   from the ethane controlled release test near Denver, Colorado on November 19, 2014. It is evident
355   from both the simulation data and the field data that a statistically stable estimate seems to be
356   achieved somewhere between 20-25 loops around the source.

3.7 Discretization and Altitude Binning the Flux Divergence Data

358   Measurements of the relevant scalars (e.g. CH_4) and meteorological variables are sampled at discrete
359   time intervals. For our analyses, we interpolate all measurements including GPS (3 Hz), methane (1
360   Hz), temperature (1 Hz) and computed variables including horizontal wind (1 Hz), and air density (1
361   Hz) onto a synchronous 1 Hz time series. Next, we estimate the path integral for each individual loop
362   of the flux normal to the flight path by summing up the flux contributions times the sample length
363   around each loop and then summing over the height intervals,

$$Q_c = \left\langle \frac{\partial m}{\partial t} \right\rangle + \oiint \boldsymbol{F_c} \cdot \hat{\boldsymbol{n}} \, dS = \frac{\Delta m}{\Delta t} + \sum_{z=0}^{z=Z_t} \left(\sum_{0}^{L} (\rho \cdot u_n) \cdot \Delta s \right) \cdot \Delta z, \qquad (9)$$

364   where ρ is the scalar air density, u_n is the wind speed normal to the flight path, Δs is the distance
365   covered during the 1 s time interval of each measurement and *L* is the distance covered in one
366   complete circuit. The outer summation sums each of the discrete vertical laps from the bottom (*z* =
367   0) to the highest lap (*z* = z_t). If all laps were sampled at equidistant altitudes, the total divergence
368   could be calculated as the average divergence of all laps multiplied by the top altitude. However,
369   because there is greater horizontal transport and variability at lower altitudes, as demonstrated by
370   the widening standard deviations approaching the surface in the theoretical flux divergence profiles
371   shown in Figure 4, more sampling laps at lower altitudes increase the statistical validity of the largest
372   horizontal transport values. To ensure that all altitudes are nearly equally weighted, we divide the
373   vertical range into six equally spaced bins, save for the lowest bin which is extended to the surface,
374   and then average the measurements from the laps within each bin. The total emission is the sum of
375   the flux times the path length in each bin multiplied by the bin width. We also performed 6 flights

376 where we sampled equally at all altitudes to allow a comparison of the direct average versus the
377 binned results, and in all of these flights the values derived by the two methods agreed to within 5%.

378 **3.8   Error Analysis**

379 Our method assumes a stationary emission source. The leg-to-leg variability is primarily driven by the
380 stochastic nature of turbulence (e.g. we may sample the plume on one lap and miss it on another). By
381 aggregating the laps into vertical bins, we can use the standard deviation of the horizontal fluxes
382 within each bin as an estimate of the uncertainty within that bin. Then the total uncertainty in the
383 estimate of the flux divergence is simply estimated by adding up the individual bin uncertainties in
384 quadrature. The first term on the rhs of Equation 6 is the time rate of change of the scalar mass
385 within the cylindrical flight volume. This storage term is estimated by performing a least squares fit of
386 the methane density with time and altitude. The resulting uncertainty in the time rate of change is
387 then combined (summed in quadrature) with the uncertainty from the altitude bins to achieve a total
388 uncertainty in the measurement.
389
390 **4   Results and Discussion**
391
392 We use measurements from three sets of flights to characterize the accuracy of this estimation
393 method. We flew 2 days measuring an ethane controlled release provided by Aerodyne Research,
394 Inc., 4 days measuring a natural gas controlled release provided by the Pacific Gas & Electric Company
395 (PG&E), and 6 power-plant flights where our estimates are compared with reported hourly power
396 plant CO_2 emissions.
397
398

399 **4.1   Ethane Controlled Releases**

400 Two experiments with known/controlled ethane releases were performed in collaboration with the
401 Aerodyne Mobile Laboratory team. Pure ethane was released and measured with a flowmeter by the
402 Aerodyne ground crew. The Colorado site (November, 2014) was in a remote area approximately 105
403 miles NE of Denver. This site was chosen because of the flat terrain and lack of other nearby ethane
404 sources that could pollute the controlled release plume. The flux profiles for both releases are shown
405 in Figure 8 and indicate that, in both cases, the aircraft successfully flew above the ethane plume
406 (measurements tend toward zero with increasing altitude). An example of an individual lap is shown
407 in Figure 9 and indicates a clear plume signal downwind of the release. As the aircraft climbs,
408 eventually the signal disappears, as shown in the figure. Agreement was excellent, with the
409 estimated emission just 2% over the actual controlled release rate.   The second Aerodyne controlled
410 release in Arkansas on October 3, 2015 was performed at a site surrounded by nearby emission
411 sources and an elevation change (~70m) within the aircraft flight path. The aircraft-derived ethane
412 emission estimate was 25% higher than the controlled release rate and the calculated uncertainty
413 was significantly higher than on other sites (Table 2).

414 A significant upwind ethane source was observed during the Arkansas experiment. This source was
415 evident on roughly half of the upwind passes, suggesting that techniques which rely on a limited
416 number of upwind passes to characterize the background could have a large random error and thus
417 erroneously estimate the upwind source strength. A similar problem would affect those techniques
418 that employ a downwind transect, using the edges of that transect lying outside the plume to
419 estimate the background concentration. These observations demonstrate the complication (and
420 bias) that can arise from nearby sources. Since this method integrates all the emission sources in the
421 area within the flight circle and a small distance upwind of the circle depending on the vertical
422 mixing, estimates from Gauss's method may be biased high if there are sources within that area. The
423 average error of the two ethane releases is 13%.
424

425 **4.2   Natural Gas Controlled Releases**

426 In conjunction with PG&E, we performed two sets of two-day ground-level controlled release
427 experiments from existing PG&E facilities, exactly one year apart. The first set was performed
428 southeast of Sacramento near the town of Rio Vista, CA at the Rio Vista "Y" station and the second
429 set near Bakersfield, CA. For the Rio Vista test, the release rate was not calibrated with a flow meter
430 but, based on the size of the orifice and the upstream pressure, the release rate was estimated at
431 15.2 ± 1.5 kg hr^{-1}. This release rate is an estimate of the total gas being released which is a
432 combination of primarily CH_4 and C_2H_6. We use the regression fit of ethane to methane (averaging
433 0.085 by mass) to estimate the actual release rate of each scalar.

434 In comparison with the C_2H_6 controlled release, CH_4 controlled releases suffer from the effect of small
435 enhancements relative to the background concentration. During the Rio Vista release, the largest
436 enhancement that we measured was 100 ppb, with 30-40 ppb being typical. Using a typical
437 background level of 1.9 ppm, a 40 ppb enhancement represents 2% of the background. In contrast,
438 for ethane the enhancements are as large or larger than the background.   The results of the methane
439 controlled release tests are shown in Table 3 and indicate aircraft-derived estimates within 17% of
440 the controlled release rate. This large background results in increased uncertainty in the emission
441 calculation. The average difference between the estimated emission and the calculated flow rate is
442 13%.
443

444 **4.3   Power Plant Flights**

445 Power plants in the U.S. are required to report CO_2 emissions to EPA (https://ampd.epa.gov/ampd)
446 on an hourly basis. The accuracy of the reported CO_2 emissions has been determined to be ±10.8-
447 11.0% based on reported U.S. average differences between Energy Information Administration (EIA)
448 fuel-based estimates and EPA continuous emission monitoring-based estimates (Ackerman and
449 Sundquist, 2008; Peischl et al., 2010; Quick, 2014). Also, Peischl et al. (2010) determined an accuracy
450 of power plants reporting CO_2 emissions in Texas of ±14.0% based on differences between observed
451 downwind SO_2/CO_2 and NOx/CO_2 emission ratios and those reported via EPA continuous emission
452 monitoring (Peischl et al., 2010). Here, we use the slightly larger uncertainty from Peischl et al.

453 (2010). Power plant emissions are "hot" gases and very buoyant, in contrast to a surface emission
454 source that is typically not buoyant. An additional uncertainty arises from temporal emission
455 variability (hourly averaged reported CO_2 emissions vs. <1 hr power plant flights that may cover parts
456 of two reported consecutive hourly values). We estimate the total reported uncertainty by summing
457 in quadrature the Peischl estimate and the relative difference between two reported consecutive
458 hourly CO_2 emission values closest to the time of the power plant sampling. The aircraft frequently
459 encountered power plants during oil & gas monitoring campaigns, but usually did not have the flight
460 time to perform a full emissions characterization of the power plant. Here we limit our comparison
461 to days when the aircraft performed a minimum of 10 laps around the plant, thus excluding the quick
462 fly-bys where uncertainties would be unacceptably large. The results are presented in Table 4 and
463 indicate very good agreement between Gauss's method and the reported CO_2 emissions with the
464 averaged difference being 10.6%.   A comparison plot of the reported versus measured CO_2 emissions
465 is shown in Figure 10. The average difference between the reported and measured emissions for the
466 5 power plants is 11%.

467

5   Conclusion

469 This technique was developed out of the necessity to identify and quantify individual well pads in an
470 extensive oil and gas production field. Consequently the frequent tracking of the upwind and
471 downwind side of the source provides a very accurate determination of the location and magnitude
472 of a given emission site. The main uncertainty arises from the effluent below the lowest flight
473 altitude, but this is minimized by targeting a downwind distance determined by LES studies to provide
474 very little change in the plume flux divergence from the lowest loop to the ground. In addition to the
475 controlled release experiments, hundreds of sites have been measured using this technique with
476 varying levels of success. Ideal conditions include flat terrain, ample sunlight to promote vertical
477 mixing, consistent winds, and no nearby competing sources. Under optimal conditions we have
478 demonstrated that measurement uncertainties are quite low, often better than 10%. As the
479 conditions deteriorate from the ideal to situations involving complex terrain, variable winds or nearby
480 upwind sources, measured uncertainties can increase to be as large or larger than the emission
481 estimates themselves. In the worst case of stably stratified conditions (winter or night time), for
482 instance, the lack of vertical mixing may preclude the trace gases emitted at the surface from
483 reaching the minimum safe flight altitude. Complex terrain provides a challenge to the method
484 because the aircraft is unable to maintain a constant altitude above the ground. A possible future
485 refinement of this technique to be applied in complex terrain would be to fit the measurements of
486 both wind and mixing ratio to a uniform 3-dimensional surface surrounding the source, where the
487 grid passes through the terrain and then integrate the flux normal to this irregular virtual flight path.
488 This would not assume level loop flight legs and would, in principle, account for individual loops being
489 flown at differing altitudes and thus more closely track mass continuity near the terrain elevation.

490

Simulation	Δx, Δy (m)	Lx, Ly (km)	ΔZ (km)	Δt (s)	Δz (m)	CBL Depth (m)	CBL mean wind (ms^{-1})	w_* (ms^{-1})	$-z_i/L_{MO}$	X_{max}
UCD50A	50	8	2.5	0.30	8	750	2	0.92	210	4.5
UCD50B	50	8	2.5	0.30	8	600	3.8	0.86	73	3.6
UCD40	40	6	2.5	0.24	10	850	4.5	0.96	53	2.4

Table 1 - Domain and micrometeorological parameters for the three WRF-LES experiments in this study. *L* represents the Monin-Obukhov length.

Experiment Location	Date	Laps	Released CH_4 kg hr^{-1}	Estimated CH_4 kg hr^{-1}	Released C_2H_6 kg hr^{-1}	Estimated C_2H_6 kg hr^{-1}	Ethane Difference
Colorado	2014-Nov-19	50	0.0	-0.1±0.3	5.5±0.5	5.6±2.9	+2%
Arkansas	2015-Oct-03	19	0.0	-3.4±12.3	8.1±0.8	10.0±6.1	+24%

Table 2 - Ethane controlled releases.

Experiment Location	Date	Laps	Released CH_4 kg hr^{-1}	Estimated CH_4 kg hr^{-1}	Released C_2H_6 kg hr^{-1}	Estimated C_2H_6 kg hr^{-1}	Methane Difference
Rio Vista	2014-Nov-03	37	13.9±2.8	12.8±8.5	1.2±0.5	0.6±0.4	-8%
Rio Vista	2014-Nov-04	27	13.9±2.8	11.5±3.2	1.2±0.5	0.5±0.3	-17%

Table 3 - Natural Gas controlled release

Power Plant	Date	Hour UTC	Laps	Reported CO_2 T hr^{-1}	Estimated CO_2 T hr^{-1}	Difference
Rocky Mountain Energy	2014-Oct-06	20	19	99±14	111±24	13%
Saint Vrain	2014-Oct-04	19	21	124±17	122±41	-1%
Pawnee	2014-Nov-19	20	14	575±81	555±160	-3%
Saint Vrain	2015-Sep-17	20	14	361±54	280±115	-23%
Four Corners Power Plant	2015-Apr-11	18	12	1289±387	1119±343	-13%

Table 4 - Power Plant estimates. The mid-point of the measurements (hours UTC) is indicated in the third column (Hour). The reported emissions from the hour before to the hour after that time were averaged to derive the "Reported" emissions in column 5. Emissions are reported in units of metric tons (T) per hour.

4. Acknowledgements

Funding for this study provided by the California Energy Commission (CEC) and the US Department of Energy (DOE). Funding for the Denver and Arkansas portion of this work was provided by RPSEA/NETL contract no 12122-95/DE-AC26-07NT42677 to the Colorado School of Mines. Cost sharing was provided by Colorado Energy Research Collaboratory, the National Oceanic and Atmospheric Administration Climate Program Office, the National Science Foundation (CBET-1240584), Southwestern Energy, XTO, Chevron, Statoil and the American Gas Association, many of whom also provided operational data and/or site access. We also thank Professor Shuhua Chen for assistance with the WRF-LES code modifications and advice. The National Center for Atmospheric Research is sponsored by the National Science Foundation. This work was supported in part by the NOAA AC4 program under grant NA14OAR0110139 and the Bureau of Land Management, Grant L15PG00058. We thank Ying Pan for her significant contribution to our understanding of the negative horizontal scalar flux.
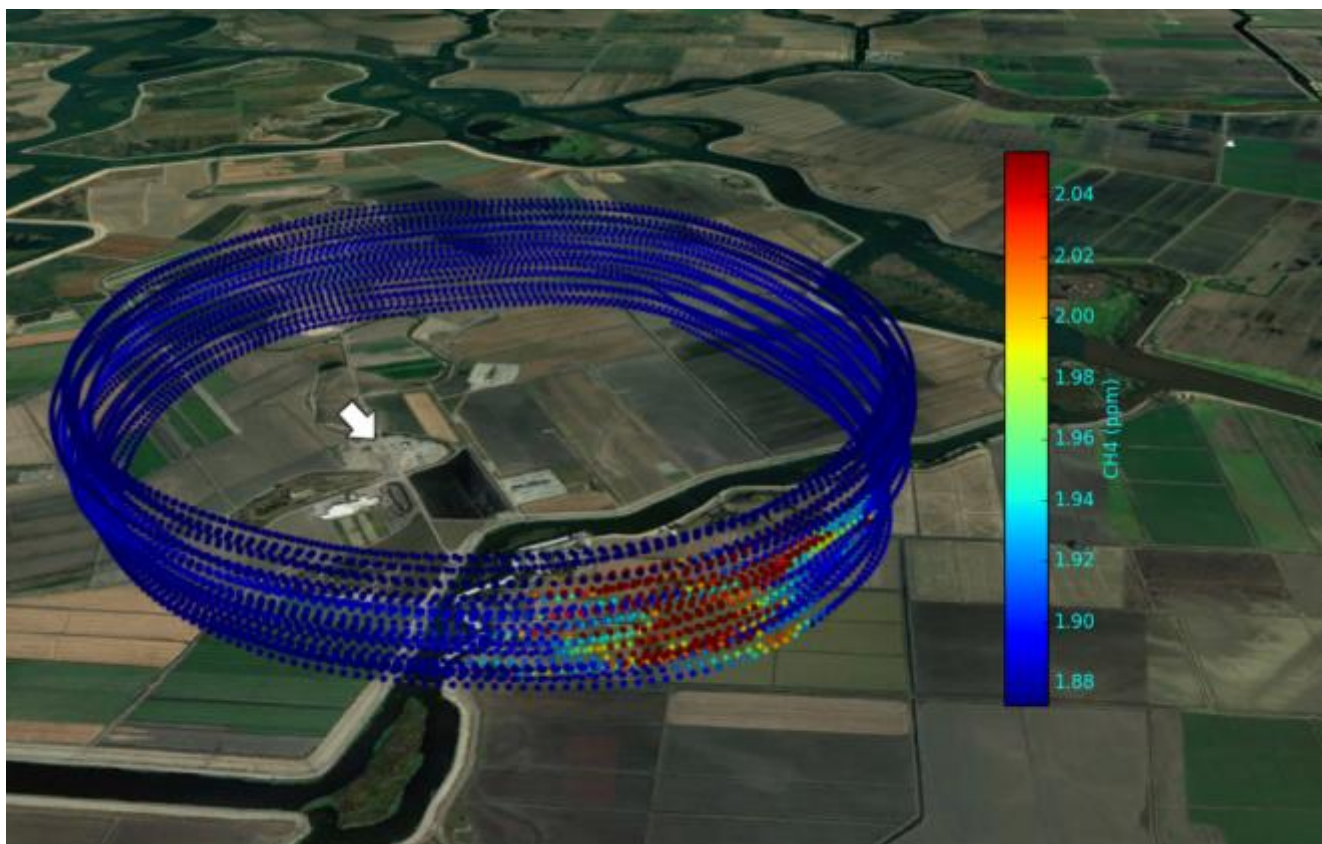
Figure 1 - Map of the airplane flight pattern sampling a methane plume emanating from an underground storage facility. Wind direction is indicated by the white arrow and the methane mixing ratio is given by the color bar to the right. This flight was conducted on June 28, 2016 and took place between 12:46PM and 1:52PM LT at altitudes ranging from 91 m to 560 m with a loop diameter of approximately 3 km. The measured methane emission rate was 763±127 kg hr^{-1}.
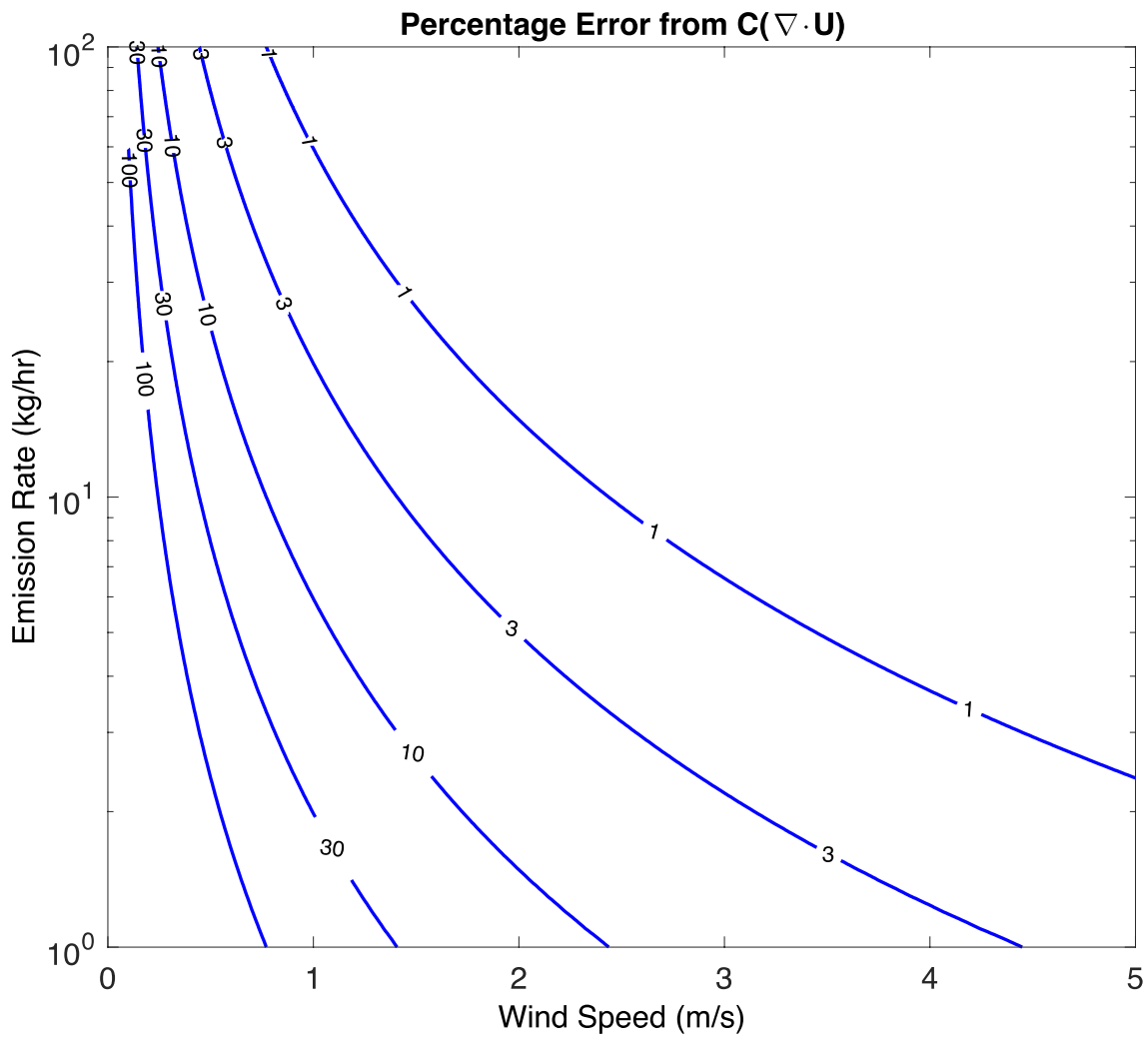
Figure 2 - Graphical representation of the relative magnitude (%) of the contribution of the horizontal wind divergence to the horizontal advective terms in Equation 3, as a function of wind speed and source magnitude for methane, using a typical global background of 1.9 ppm and divergence of 10^{-5} s^{-1}.
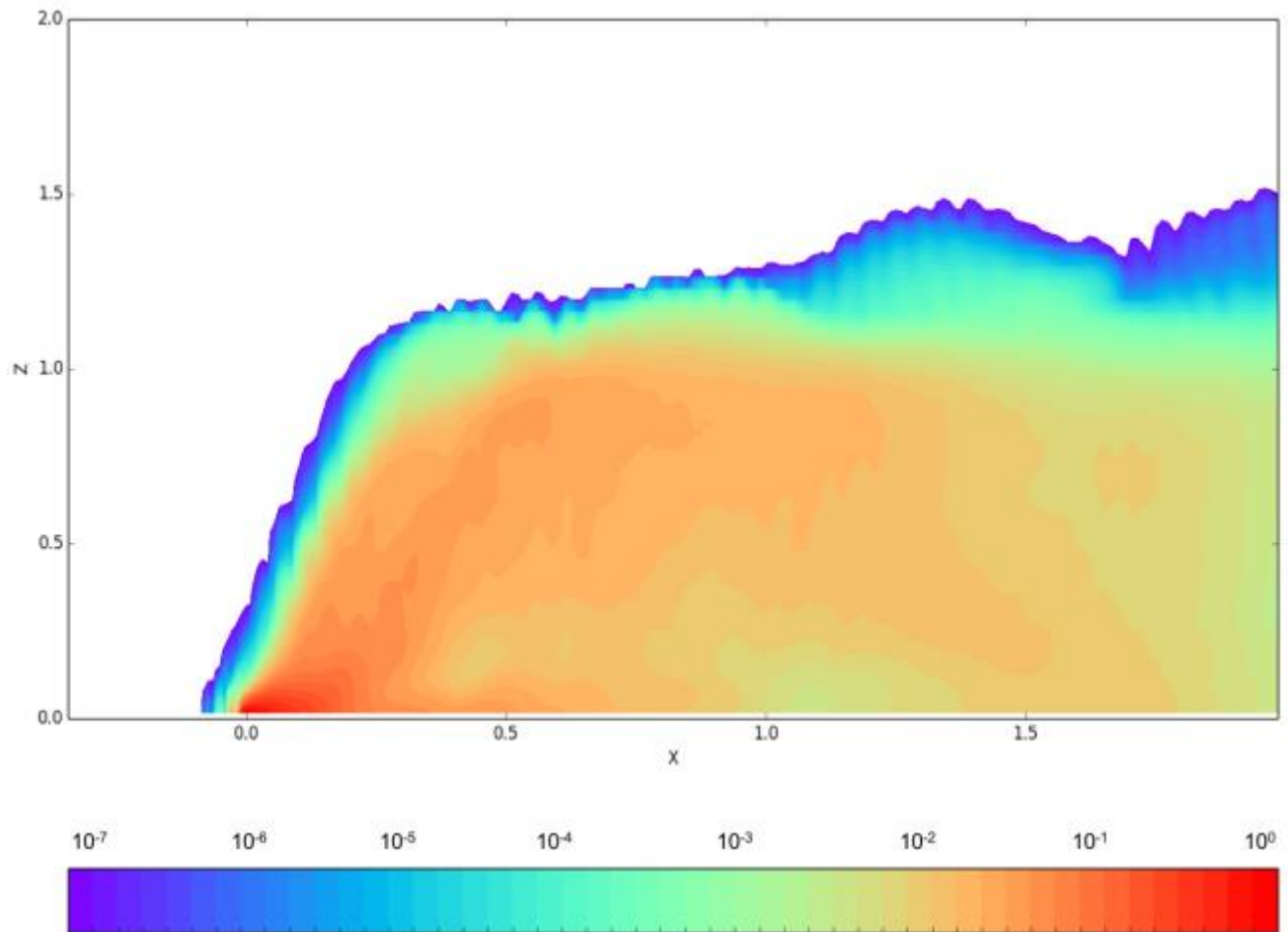
Figure 3 Relative cross wind integrated concentrations of an effluent plume released at the surface in the UCD50B simulation. The data are averaged over 15 minutes of simulation time and normalized by the maximum concentration.
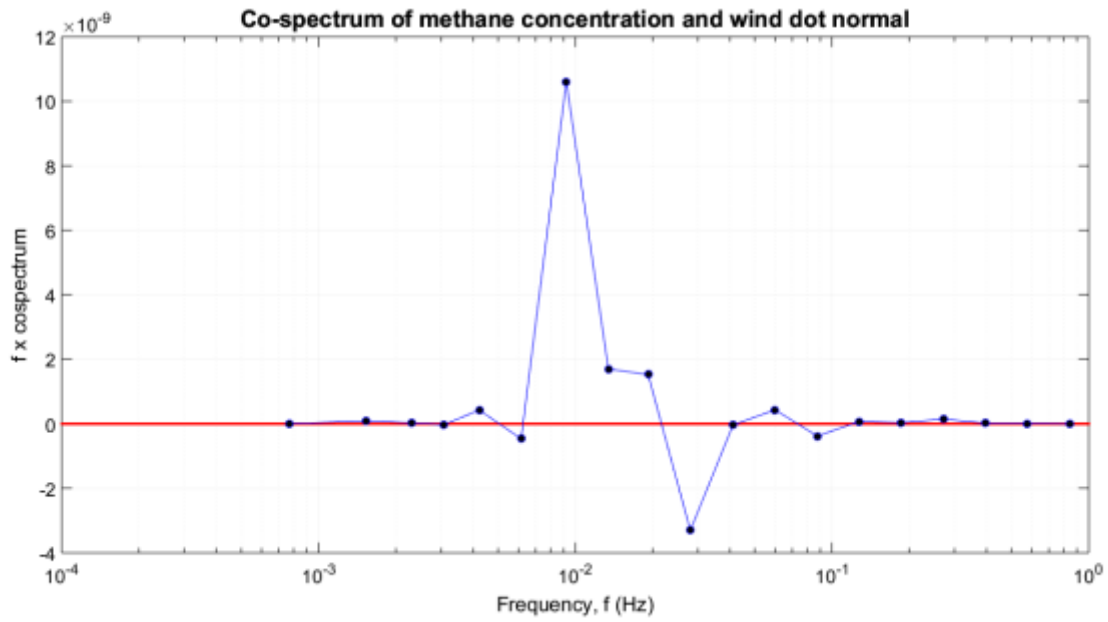
Figure 4 Average cospectrum of the outward directed component of the observed wind and the methane concentration from 70 laps around a point source near San Antonio, Texas. The peak at 10^{-2} Hz corresponds to the period of the circle.
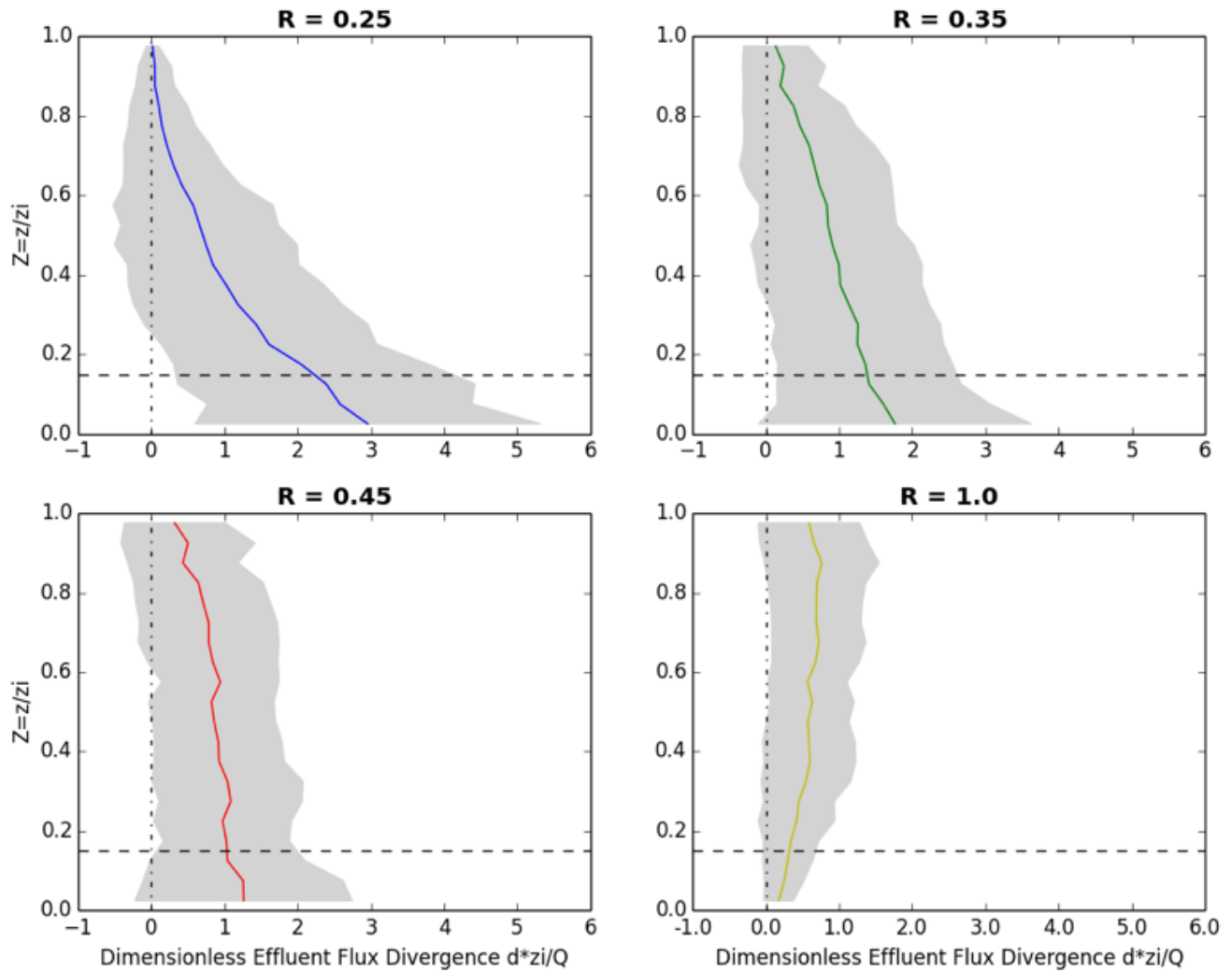
Figure 5 Dimensionless flux divergence profiles generated from averaging over 3 different WRF-LES runs using 30 time steps for each one. The horizontal flux per unit altitude ($d = F/\Delta z$) is normalized by the boundary layer height, z_i, and source strength, Q. The colored profiles are averages at various dimensionless distances, R=0.1, 0.2, 0.3, and 0.4 and the gray areas represent one standard deviation about the mean. The horizontal dashed lines are the approximate lowest safe flight altitude.
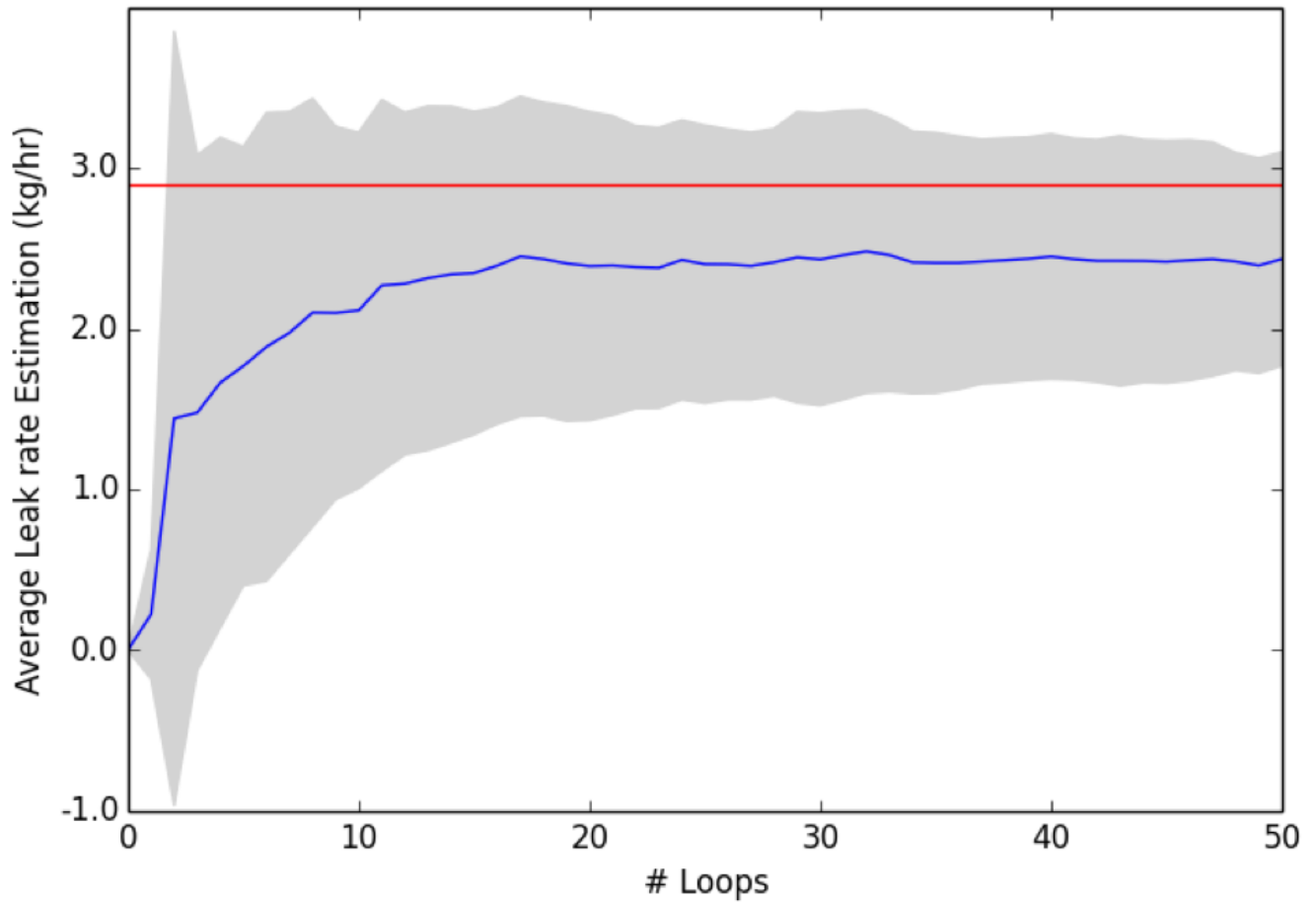
Figure 6 Rate of convergence toward the final leak rate estimation as a function of the number of loops for LES CASE UCD508. By 15 laps, the emissions estimate (blue line) has stabilized to 2.5 kg hr^{-1} compared to the actual leak rate (red line) of 2.9 kg hr^{-1}. Dimensionless distance R = 0.25, 50 realizations. Grey area represents 1 standard deviation.

.
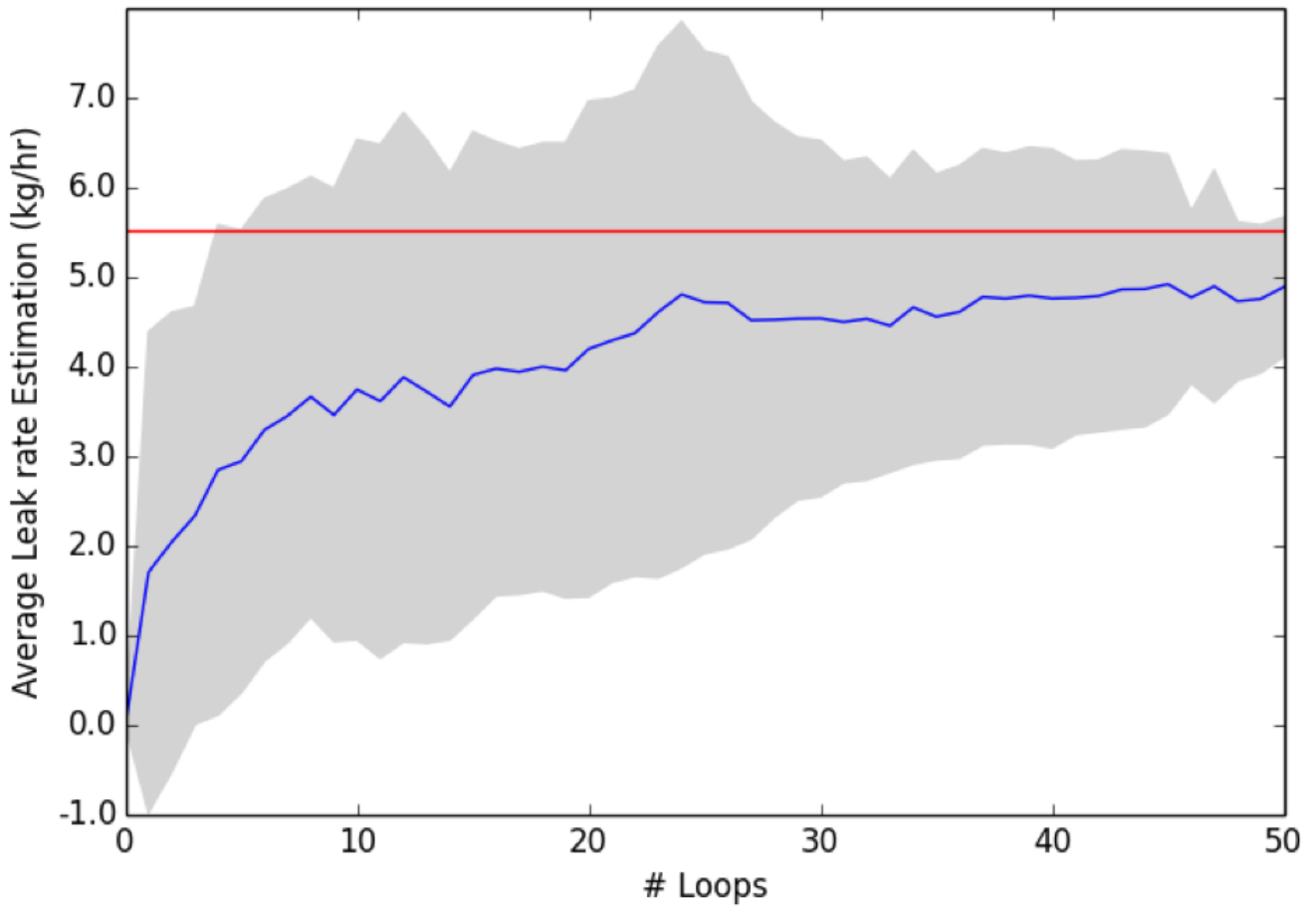
Figure 7 Averaged LES estimates for the Aerodyne case. This leak shows a slightly higher number of laps before convergence (~25 laps).   This simulation was performed using the conditions for the Aerodyne controlled release near Denver, Colorado on November 19, 2014.
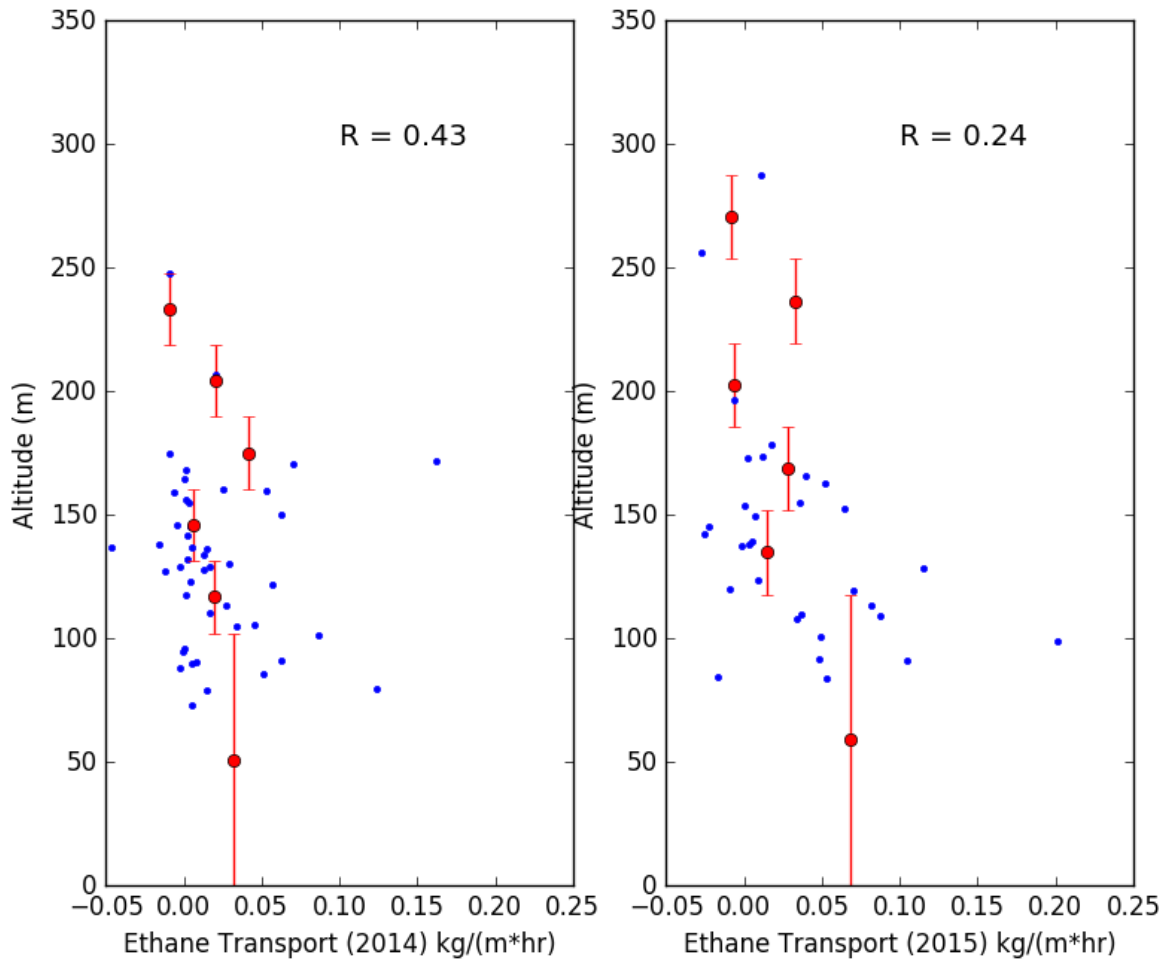
Figure 8 - Ethane horizontal transport profiles for the Aerodyne controlled releases near Denver, Colorado on November 19, 2014 (left) and in Bee Branch, Arkansas on October 3, 2015 (right). Blue dots represent individual flight loop measurements and the red circles represent the bin average values for altitude intervals represented by the red bars.
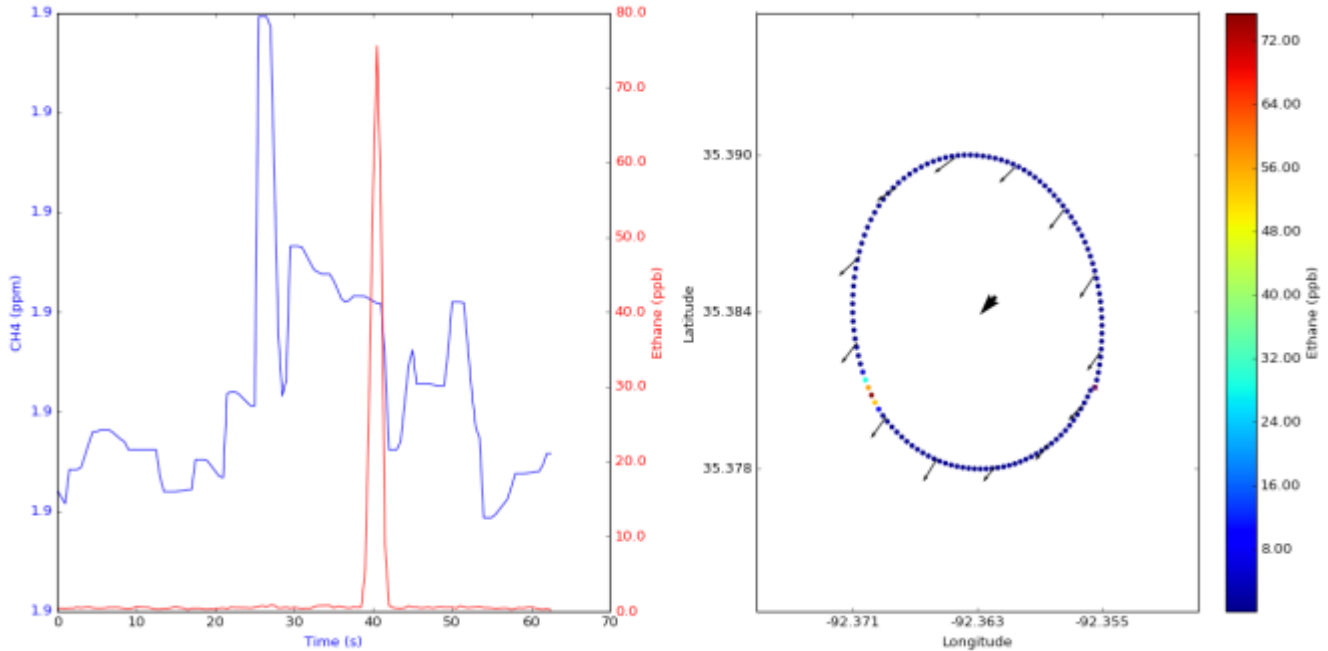
Figure 9 (Left plot) Time series of methane (blue) and ethane (red) along with (right plot) the geographic distribution of ethane (colorbar) and instantaneous winds (arrows) from a single flight loop during the second ethane controlled release.
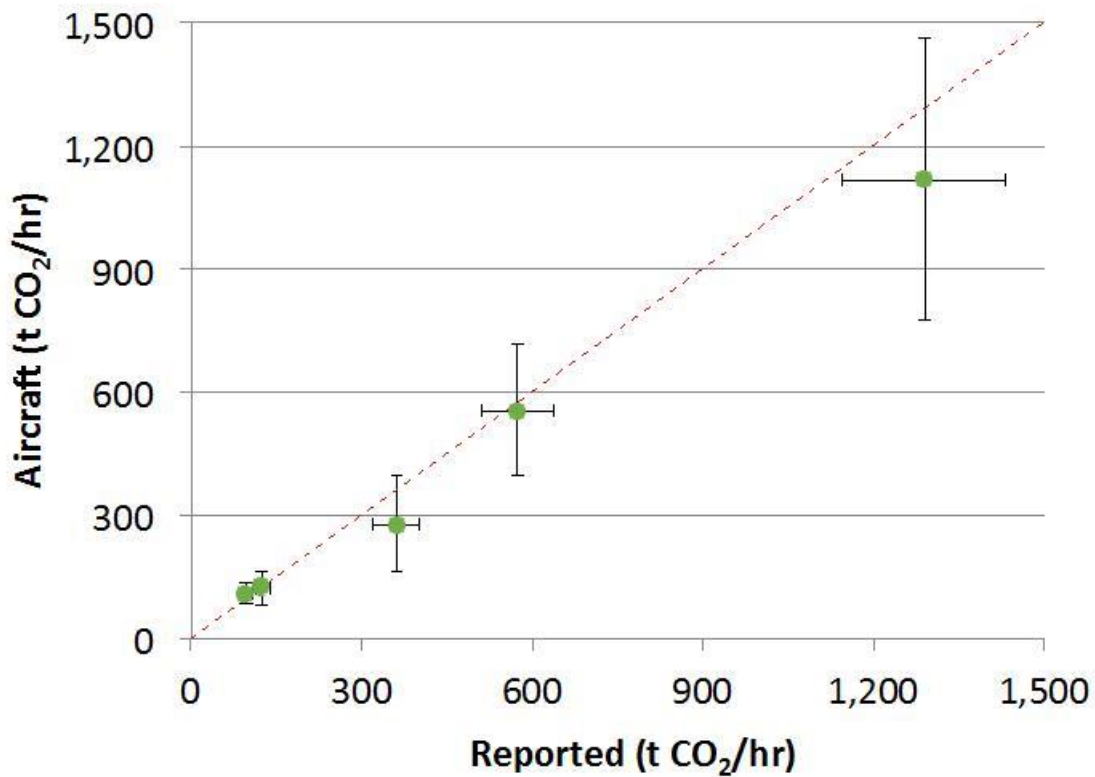
Figure 10 Comparison of aircraft versus reported power plant emissions.

Ackerman, K. V. and Sundquist, E. T.: Comparison of two US power-plant carbon dioxide emissions data sets, Environmental Science & Technology, 42, 5688-5693, 2008.

Alfieri, J. G. and Blanken, P. D.: How representative is a point? The spatial variability of flux measurements across short distances. In: Remote Sensing and Hydrology, Neale, C. M. U. and Cosh, M. H. (Eds.), IAHS Publication, 2012.

Alfieri, J. G., Kustas, W. P., Prueger, J. H., Hipps, L. E., Evett, S. R., Basara, J. B., Neale, C. M. U., French, A. N., Colaizzi, P., Agam, N., Cosh, M. H., Chavez, J. L., and Howell, T. A.: On the discrepancy between eddy covariance and lysimetry-based surface flux measurements under strongly advective conditions, Advances in Water Resources, 50, 62-78, 2012.

Bergamaschi, P., Krol, M., Dentener, F., Vermeulen, A., Meinhardt, F., Graul, R., Ramonet, M., Peters, W., and Dlugokencky, E. J.: Inverse modelling of national and European CH4 emissions using the atmospheric zoom model TM5, Atmospheric Chemistry and Physics, 5, 2431-2460, 2005.

Beswick, K. M., Simpson, T. W., Fowler, D., Choularton, T. W., Gallagher, M. W., Hargreaves, K. J., Sutton, M. A., and Kaye, A.: Methane emissions on large scales, Atmospheric Environment, 32, 3283-3291, 1998.

Caughey, S. J. and Palmer, S. G.: SOME ASPECTS OF TURBULENCE STRUCTURE THROUGH THE DEPTH OF THE CONVECTIVE BOUNDARY-LAYER, Quarterly Journal of the Royal Meteorological Society, 105, 811-827, 1979.

Caulton, D. R., Shepson, P. B., Santoro, R. L., Sparks, J. P., Howarth, R. W., Ingraffea, A. R., Cambaliza, M. O. L., Sweeney, C., Karion, A., Davis, K. J., Stirm, B. H., Montzka, S. A., and Miller, B. R.: Toward a better understanding and quantification of methane emissions from shale gas development, Proceedings of the National Academy of Sciences, 111, 6237-6242, 2014.

Chang, R. Y. W., Miller, C. E., Dinardo, S. J., Karion, A., Sweeney, C., Daube, B. C., Henderson, J. M., Mountain, M. E., Eluszkiewicz, J., Miller, J. B., Bruhwiler, L. M. P., and Wofsy, S. C.: Methane emissions from Alaska in 2012 from CARVE airborne observations, Proceedings of the National Academy of Sciences of the United States of America, 111, 16694-16699, 2014.

Conley, S., Franco, G., Faloona, I., Blake, D. R., Peischl, J., and Ryerson, T. B.: Methane emissions from the 2015 Aliso Canyon blowout in Los Angeles, CA, Science, 351, 1317-1320, 2016.

Conley, S. A., Faloona, I. C., Lenschow, D. H., Karion, A., and Sweeney, C.: A Low-Cost System for Measuring Horizontal Winds from Single-Engine Aircraft, Journal of Atmospheric and Oceanic Technology, 31, 1312-1320, 2014.

Crosson, E. R.: A cavity ring-down analyzer for measuring atmospheric levels of methane, carbon dioxide, and water vapor, Applied Physics B-Lasers and Optics, 92, 403-408, 2008.

Czepiel, P. M., Mosher, B., Harriss, R. C., Shorter, J. H., McManus, J. B., Kolb, C. E., Allwine, E., and Lamb, B. K.: Landfill methane emissions measured by enclosure and atmospheric tracer methods, Journal of Geophysical Research-Atmospheres, 101, 16711-16719, 1996.

Denmead, O. T., Harper, L. A., Freney, J. R., Griffith, D. W. T., Leuning, R., and Sharpe, R. R.: A mass balance method for non-intrusive measurements of surface-air trace gas exchange, Atmospheric Environment, 32, 3679-3688, 1998.

Gallagher, M. W., Choularton, T. W., Bower, K. N., Stromberg, I. M., Beswick, K. M., Fowler, D., and Hargreaves, K. J.: MEASUREMENTS OF METHANE FLUXES ON THE LANDSCAPE SCALE FROM A WETLAND AREA IN NORTH SCOTLAND, Atmospheric Environment, 28, 2421-2430, 1994.

Gerbig, C., Lin, J. C., Wofsy, S. C., Daube, B. C., Andrews, A. E., Stephens, B. B., Bakwin, P. S., and Grainger, C. A.: Toward constraining regional-scale fluxes of CO2 with atmospheric observations over a continent: 2. Analysis of COBRA data using a receptor-oriented framework, Journal of Geophysical Research-Atmospheres, 108, 27, 2003.

Gordon, M., Li, S. M., Staebler, R., Darlington, A., Hayden, K., O'Brien, J., and Wolde, M.: Determining air pollutant emission rates based on mass balance using airborne measurement data over the Alberta oil sands operations, Atmos. Meas. Tech., 8, 3745-3765, 2015.

Hacker, J. M., Chen, D. L., Bai, M., Ewenz, C., Junkermann, W., Lieff, W., McManus, B., Neininger, B., Sun, J. L., Coates, T., Denmead, T., Flesch, T., McGinn, S., and Hill, J.: Using airborne technology to quantify and apportion emissions of CH4 and NH3 from feedlots, Animal Production Science, 56, 190-203, 2016.

Hiller, R. V., Neininger, B., Brunner, D., Gerbig, C., Bretscher, D., Kunzle, T., Buchmann, N., and Eugster, W.: Aircraft-based CH4 flux estimates for validation of emissions from an agriculturally dominated area in Switzerland, Journal of Geophysical Research-Atmospheres, 119, 4874-4887, 2014.

Hirsch, A. I., Michalak, A. M., Bruhwiler, L. M., Peters, W., Dlugokencky, E. J., and Tans, P. P.: Inverse modeling estimates of the global nitrous oxide surface flux from 1998-2001, Global Biogeochemical Cycles, 20, 2006.

Kalthoff, N., Corsmeier, U., Schmidt, K., Kottmeier, C., Fiedler, F., Habram, M., and Slemr, F.: Emissions of the city of Augsburg determined using the mass balance method, Atmospheric Environment, 36, S19-S31, 2002.

Karion, A., Sweeney, C., Kort, E. A., Shepson, P. B., Brewer, A., Cambaliza, M., Conley, S. A., Davis, K., Deng, A. J., Hardesty, M., Herndon, S. C., Lauvaux, T., Lavoie, T., Lyon, D., Newberger, T., Petron, G., Rella, C., Smith, M., Wolter, S., Yacovitch, T. I., and Tans, P.: Aircraft-Based Estimate of Total Methane Emissions from the Barnett Shale Region, Environmental Science & Technology, 49, 8124-8131, 2015.

Karion, A., Sweeney, C., Petron, G., Frost, G., Hardesty, R. M., Kofler, J., Miller, B. R., Newberger, T., Wolter, S., Banta, R., Brewer, A., Dlugokencky, E., Lang, P., Montzka, S. A., Schnell, R., Tans, P., Trainer, M., Zamora, R., and Conley, S.: Methane emissions estimate from airborne measurements over a western United States natural gas field, Geophysical Research Letters, 40, 4393-4397, 2013.

Lamb, B. K., McManus, J. B., Shorter, J. H., Kolb, C. E., Mosher, B., Harriss, R. C., Allwine, E., Blaha, D., Howard, T., Guenther, A., Lott, R. A., Siverson, R., Westberg, H., and Zimmerman, P.: DEVELOPMENT OF ATMOSPHERIC TRACER METHODS TO MEASURE METHANE EMISSIONS FROM NATURAL-GAS FACILITIES AND URBAN AREAS, Environmental Science & Technology, 29, 1468-1479, 1995.

Lavoie, T. N., Shepson, P. B., Cambaliza, M. O. L., Stirm, B. H., Karion, A., Sweeney, C., Yacovitch, T. I., Herndon, S. C., Lan, X., and Lyon, D.: Aircraft-Based Measurements of Point Source Methane Emissions in the Barnett Shale Basin, Environmental Science & Technology, 49, 7904-7913, 2015.

Lenschow, D. H., Savic-Jovcic, V., and Stevens, B.: Divergence and vorticity from aircraft air motion measurements, Journal of Atmospheric and Oceanic Technology, 24, 2062-2072, 2007.

Leuning, R., Freney, J. R., Denmead, O. T., and Simpson, J. R.: A SAMPLER FOR MEASURING ATMOSPHERIC AMMONIA FLUX, Atmospheric Environment, 19, 1117-1124, 1985.

Mays, K. L., Shepson, P. B., Stirm, B. H., Karion, A., Sweeney, C., and Gurney, K. R.: Aircraft-Based Measurements of the Carbon Footprint of Indianapolis, Environmental Science & Technology, 43, 7816-7823, 2009.

Miller, J. B., Lehman, S. J., Montzka, S. A., Sweeney, C., Miller, B. R., Karion, A., Wolak, C., Dlugokencky, E. J., Southon, J., Turnbull, J. C., and Tans, P. P.: Linking emissions of fossil fuel CO_2 and other anthropogenic trace gases using atmospheric (CO_2)-C-14, Journal of Geophysical Research-Atmospheres, 117, 23, 2012.

Miller, S. M., Wofsy, S. C., Michalak, A. M., Kort, E. A., Andrews, A. E., Biraud, S. C., Dlugokencky, E. J., Eluszkiewicz, J., Fischer, M. L., Janssens-Maenhout, G., Miller, B. R., Miller, J. B., Montzka, S. A., Nehrkorn, T., and Sweeney, C.: Anthropogenic emissions of methane in the United States, Proceedings of the National Academy of Sciences of the United States of America, 110, 20018-20022, 2013.

Muhle, S., Balsam, I., and Cheeseman, C. R.: Comparison of carbon emissions associated with municipal solid waste management in Germany and the UK, Resour. Conserv. Recycl., 54, 793-801, 2010.

Neef, L., van Weele, M., and van Velthoven, P.: Optimal estimation of the present-day global methane budget, Global Biogeochemical Cycles, 24, 2010.

Nisbet, E. and Weiss, R.: Top-Down Versus Bottom-Up, Science, 328, 1241-1243, 2010.

Pan, Y., Chamecki, M., and Isard, S. A.: Large-eddy simulation of turbulence and particle dispersion inside the canopy roughness sublayer, Journal of Fluid Mechanics, 753, 499-534, 2014.

Peischl, J., Ryerson, T. B., Brioude, J., Aikin, K. C., Andrews, A. E., Atlas, E., Blake, D., Daube, B. C., de Gouw, J. A., Dlugokencky, E., Frost, G. J., Gentner, D. R., Gilman, J. B., Goldstein, A. H., Harley, R. A., Holloway, J. S., Kofler, J., Kuster, W. C., Lang, P. M., Novelli, P. C., Santoni, G. W., Trainer, M., Wofsy, S. C., and Parrish, D. D.: Quantifying sources of methane using light alkanes in the Los Angeles basin, California, Journal of Geophysical Research-Atmospheres, 118, 4974-4990, 2013.

Peischl, J., Ryerson, T. B., Holloway, J. S., Parrish, D. D., Trainer, M., Frost, G. J., Aikin, K. C., Brown, S. S., Dube, W. P., Stark, H., and Fehsenfeld, F. C.: A top-down analysis of emissions from selected Texas power plants during TexAQS 2000 and 2006, Journal of Geophysical Research-Atmospheres, 115, 15, 2010.

Petron, G., Karion, A., Sweeney, C., Miller, B. R., Montzka, S. A., Frost, G. J., Trainer, M., Tans, P., Andrews, A., Kofler, J., Helmig, D., Guenther, D., Dlugokencky, E., Lang, P., Newberger, T., Wolter, S., Hall, B., Novelli, P., Brewer, A., Conley, S., Hardesty, M., Banta, R., White, A., Noone, D., Wolfe, D., and Schnell, R.: A new look at methane and nonmethane hydrocarbon emissions from oil and natural gas operations in the Colorado Denver-Julesburg Basin, Journal of Geophysical Research-Atmospheres, 119, 6836-6852, 2014.

Quick, J. C.: Carbon dioxide emission tallies for 210 U.S. coal-fired power plants: A comparison of two accounting methods, J. Air Waste Manage. Assoc., 64, 73-79, 2014.

Raupach, M. R. and Legg, B. J.: THE USES AND LIMITATIONS OF FLUX-GRADIENT RELATIONSHIPS IN MICROMETEOROLOGY, Agric. Water Manage., 8, 119-131, 1984.

Ritter, J. A., Barrick, J. D. W., Watson, C. E., Sachse, G. W., Gregory, G. L., Anderson, B. E., Woerner, M. A., and Collins, J. E.: AIRBORNE BOUNDARY-LAYER FLUX MEASUREMENTS OF TRACE SPECIES OVER CANADIAN BOREAL FOREST AND NORTHERN WETLAND REGIONS, Journal of Geophysical Research-Atmospheres, 99, 1671-1685, 1994.

Roscioli, J. R., Yacovitch, T. I., Floerchinger, C., Mitchell, A. L., Tkacik, D. S., Subramanian, R., Martinez, D. M., Vaughn, T. L., Williams, L., Zimmerle, D., Robinson, A. L., Herndon, S. C., and Marchese, A. J.: Measurements of methane emissions from natural gas gathering facilities and processing plants: measurement methods, Atmos. Meas. Tech., 8, 2017-2035, 2015.

Ryerson, T. B., Buhr, M. P., Frost, G. J., Goldan, P. D., Holloway, J. S., Hubler, G., Jobson, B. T., Kuster, W. C., McKeen, S. A., Parrish, D. D., Roberts, J. M., Sueper, D. T., Trainer, M., Williams, J., and Fehsenfeld, F. C.: Emissions lifetimes and ozone formation in power plant plumes, Journal of Geophysical Research-Atmospheres, 103, 22569-22583, 1998.

Ryerson, T. B., Trainer, M., Holloway, J. S., Parrish, D. D., Huey, L. G., Sueper, D. T., Frost, G. J., Donnelly, S. G., Schauffler, S., Atlas, E. L., Kuster, W. C., Goldan, P. D., Hubler, G., Meagher, J. F., and Fehsenfeld, F. C.: Observations of ozone formation in power plant plumes and implications for ozone control strategies, Science, 292, 719-723, 2001.

Stull, R. B.: An Introduction to Boundary Layer Meteorology, Kluwer Academic Publishers, 1988.

Taylor, G. I.: Diffusion by Continuous Movements, Proceedings of the London Mathematical Society, s2-20, 196-212, 1922.

Tratt, D. M., Buckland, K. N., Hall, J. L., Johnson, P. D., Keim, E. R., Leifer, I., Westberg, K., and Young, S. J.: Airborne visualization and quantification of discrete methane sources in the environment, Remote Sensing of Environment, 154, 74-88, 2014.

Turnbull, J. C., Karion, A., Fischer, M. L., Faloona, I., Guilderson, T., Lehman, S. J., Miller, B. R., Miller, J. B., Montzka, S., Sherwood, T., Saripalli, S., Sweeney, C., and Tans, P. P.: Assessment of fossil fuel carbon dioxide and other anthropogenic trace gas emissions from airborne measurements over Sacramento, California in spring 2009, Atmospheric Chemistry and Physics, 11, 705-721, 2011.

Wecht, K. J., Jacob, D. J., Frankenberg, C., Jiang, Z., and Blake, D. R.: Mapping of North American methane emissions with high spatial resolution by inversion of SCIAMACHY satellite data, Journal of Geophysical Research-Atmospheres, 119, 7741-7756, 2014.

Weil, J. C.: Dispersion in the Convective Boundary Layer. In: Lectures on Air Pollution Modeling, Venkatram, A. and Wyngaard, J. C. (Eds.), American Meteorological Society, Boston, MA, 1988.

Weil, J. C., Sullivan, P. P., Patton, E. G., and Moeng, C.-H.: Statistical Variability of Dispersion in the Convective Boundary Layer: Ensembles of Simulations and Observations, Boundary-Layer Meteorology, 145, 185-210, 2012.

White, W. H., Anderson, J. A., Blumenthal, D. L., Husar, R. B., Gillani, N. V., Husar, J. D., and Wilson, W. E., Jr.: Formation and Transport of Secondary Air Pollutants: Ozone and Aerosols in the St. Louis Urban Plume, Science, 194, 187-189, 1976.

Wilczak, J. M. and Bedard, A. J.: A new turbulence microbarometer and its evaluation using the budget of horizontal heat flux, Journal of Atmospheric and Oceanic Technology, 21, 1170-1181, 2004.

Willis, G. E. and Deardorff, J. W.: LABORATORY MODEL OF DIFFUSION INTO CONVECTIVE PLANETARY BOUNDARY-LAYER, Quarterly Journal of the Royal Meteorological Society, 102, 427-445, 1976.

Wilson, J. D. and Shum, W. K. N.: A REEXAMINATION OF THE INTEGRATED HORIZONTAL FLUX METHOD FOR ESTIMATING VOLATILIZATION FROM CIRCULAR PLOTS, Agric. For. Meteorol., 57, 281-295, 1992.

Wratt, D. S., Gimson, N. R., Brailsford, G. W., Lassey, K. R., Bromley, A. M., and Bell, M. J.: Estimating regional methane emissions from agriculture using aircraft measurements of concentration profiles, Atmospheric Environment, 35, 497-508, 2001.

Wyngaard, J. C.: Turbulence in the Atmosphere, Cambridge University Press, 2010.

Wyngaard, J. C., Cote, O. R., and Izumi, Y.: LOCAL FREE CONVECTION, SIMILARITY, AND BUDGETS OF SHEAR STRESS AND HEAT FLUX, Journal of the Atmospheric Sciences, 28, 1171-&, 1971.

Yacovitch, T. I., Herndon, S. C., Roscioli, J. R., Floerchinger, C., McGovern, R. M., Agnese, M., Petron, G., Kofler, J., Sweeney, C., Karion, A., Conley, S. A., Kort, E. A., Nahle, L., Fischer, M., Hildebrandt, L., Koeth, J., McManus, J. B., Nelson, D. D., Zahniser, M. S., and Kolb, C. E.: Demonstration of an Ethane Spectrometer for Methane Source Identification, Environmental Science & Technology, 48, 8028-8034, 2014.

Yuan, B., Kaser, L., Karl, T., Graus, M., Peischl, J., Campos, T. L., Shertz, S., Apel, E. C., Hornbrook, R. S., Hills, A., Gilman, J. B., Lerner, B. M., Warneke, C., Flocke, F. M., Ryerson, T. B., Guenther, A. B., and de Gouw, J. A.: Airborne flux measurements of methane and volatile organic compounds over the Haynesville and Marcellus shale gas production regions, Journal of Geophysical Research-Atmospheres, 120, 6271-6289, 2015.

Wilczak, J. M., and Bedard, A. J.: A new turbulence microbarometer and its evaluation using the budget of horizontal heat flux, J. of Atmos. & Ocean. Tech., 21, 1170-1181, 2004.

Wyngaard, J.: Turbulence in the Atmosphere, Cambridge University Press, Cambridge, 99-106, 2010.

Wyngaard, J. C. , Coté, O. R., and Izumi, Y.: Local free convection, similarity, and the budgets of shear stress and heat flux, J. Atmos. Sci., 28, 1171-1182, 1971.